COMMUNICATIONS IN COMPUTATIONAL PHYSICS
Vol. **2**, No. 5, pp. 1027-1054

Commun. Comput. Phys.
October 2007

A Semi-Lagrangian Deterministic Solver for the Semiconductor Boltzmann-Poisson System

José A. Carrillo[1,*], Armando Majorana[2] and Francesco Vecil[3]

[1] *ICREA (Institució Catalana de Recerca i Estudis Avançats) and Departament de Matemàtiques, Universitat Autònoma de Barcelona, E-08193 Bellaterra, Spain.*
[2] *Dipartimento di Matematica e Informatica, Università di Catania, Catania, Italy.*
[3] *Departament de Matemàtiques, Universitat Autònoma de Barcelona, E-08193 Bellaterra, Spain.*

Received 30 October 2006; Accepted (in revised version) 29 January 2007

Communicated by Chi-Wang Shu

Available online 27 April 2007

Abstract. In this paper we develop a deterministic numerical method for solving the Boltzmann transport equation for semiconductors based on a transport-collision time-splitting method. Transport phases are solved by means of accurate flux-balance methods while collision steps are computed in the original k-grid. Numerical experiments are shown allowing for a discussion of this method with respect to other present in the literature.

AMS subject classifications: 65M99, 82D37, 82-08

Key words: Kinetic equations for semiconductors, semi-Lagrangian schemes, splitting schemes.

1 Introduction

The semi-classical Boltzmann transport equation (BTE) is a mesoscopic description of the transport/collision of charged particles in an electronic device and is given by

$$\frac{\partial f}{\partial t}+\frac{1}{\hbar}\nabla_k\varepsilon\cdot\nabla_x f-\frac{q}{\hbar}E\cdot\nabla_k f=\mathcal{Q}[f], \tag{1.1}$$

where $f(t,x,k)$ measures the probability density of finding an electron at time t in position x with wave vector k. The parameter $\hbar$ is the Planck constant divided by 2π and q is the positive elementary charge.

*Corresponding author. *Email addresses:* carrillo@mat.uab.es (J. A. Carrillo), majorana@dmi.unict.it (A. Majorana), fvecil@mat.uab.es (F. Vecil)

The band structure of the semiconductor crystal is described by the energy-band function which can be approximated by a parabolic function given by

$$\varepsilon(k)=\frac{1}{2}\frac{\hbar^2}{m^*}|k|^2, \tag{1.2}$$

where m^* is the effective electron mass. In a first step, we shall consider the most important scattering mechanisms in Si: acoustic phonon scattering, in its elastic approximation, and optical phonon scattering with a single frequency ω. Therefore, the structure of the collision operator [20,24] is

$$\begin{aligned}\mathcal{Q}[f](t,x,k)&=\int_{\mathbb{R}^3}\left[S(k',k)f(t,x,k')-S(k,k')f(t,x,k)\right]dk'\\&=\int_{\mathbb{R}^3}S(k',k)f(t,x,k')dk'-f(t,x,k)\int_{\mathbb{R}^3}S(k,k')dk'\\&=\mathcal{Q}^+[f]-\mathcal{Q}^-[f]\end{aligned} \tag{1.3}$$

with

$$S(k,k')=K\left[(n_q+1)\delta(\varepsilon(k')-\varepsilon(k)+\hbar\omega)+n_q\delta(\varepsilon(k')-\varepsilon(k)-\hbar\omega)\right]+K_0\delta(\varepsilon(k')-\varepsilon(k)), \tag{1.4}$$

where n_q is the occupation number of phonons

$$n_q=\frac{1}{\exp\left(\frac{\hbar\omega}{k_BT_L}\right)-1}, \tag{1.5}$$

k_B is the Boltzmann constant and T_L the lattice temperature. The kernel K_0 is

$$K_0=\frac{k_BT_LE_{ac}^2}{4\pi^2\hbar{u_l}^2\rho_0}, \tag{1.6}$$

where E_{ac} is the deformation potential, u_l is the sound velocity and ρ_0 is the crystal density. The kernel K is

$$K=\frac{D_tk^2}{8\pi^2\hbar\rho_0\omega}, \tag{1.7}$$

where ω is the frequency and D_tk is the optical coupling constant. The self-consistent electrostatic field is computed through Poisson's equation

$$\Delta\Phi=\frac{q}{\epsilon}[\rho(t,x)-N_D(x)], \tag{1.8}$$

where ρ is the electron density

$$\rho(t,x)=\int_{\mathbb{R}^3}f(t,x,k)dk, \tag{1.9}$$

ϵ is the Silicon dielectric permittivity ($\epsilon=\epsilon_r\epsilon_0$ with ϵ_0 the vacuum dielectric permittivity and ϵ_r the Silicon relative dielectric permittivity), $N_D(x)$ represents the doping profile, which takes into account the injected impurities in the semiconductor lattice. The solution $\Phi(t,x)$ of Poisson's equation gives the electrostatic potential, so that the electrostatic field is given by

$$E(t,x)=-\nabla_x\Phi(t,x). \tag{1.10}$$

Further information about semiconductor modelling and related mathematical issues can be found in [17].

This system has been traditionally solved by means of Direct Simulation Monte Carlo (DSMC) methods due to the easy incorporation of new physical effects by means of adding suitable scattering operators and its efficiency in two and three-dimensional devices [24]. Nevertheless, direct deterministic numerical methods have been recently proposed in the literature [4,5,11,16,18,19] improving and complementing some features of the DSMC methods: noise-free results, detailed information of the distribution functions, transient description, different materials, see, e.g., [2,10,13]. We refer to [1,4,5,10,12] for a complete discussion of these issues and to [3] for a review of the state of the art in the deterministic numerical simulation of the Boltzmann-Poisson system.

In this work, we propose a new deterministic numerical scheme for this system. In contrast with the approach in [4,16], we work in the original coordinates (t,x,k) by using a splitting strategy decoupling transport from collision. For the transport part, we apply a semi-lagrangian numerical method based on a nonlinear local essentially non-oscillatory interpolation method recently developed in [6] for transport-like kinetic equations. The main objective of this choice is to avoid the potentially restrictive CFL condition emanating from the use of finite-differences WENO methods in energy and angular variables in [4,5] but keeping a good control of possible oscillations during the transport steps.

The collisional step is performed by interpolation from computed values on a cartesian grid to obtain the missing values of the distribution function on the surfaces of equal energy needed for the evaluation of the collision operator $\mathcal{Q}(f)$. Different interpolation procedures have been tested from the simplest and less accurate direct linear interpolation to the most advanced nonlinear local essentially non-oscillatory interpolation method in [6] as above. Conservation of mass in the collision steps is enforced by redefining the loss operator as in [2]. The different choices for interpolation in the collision step and the splitting of the operators will be discussed and compared.

This new deterministic scheme is developed in Section 2 while Section 3 is devoted to show its performance to compute steady and transient states of 1d devices and comparisons to the numerical scheme introduced in [4]. The main advantage of this scheme being the smaller number of time steps needed and the much better definition of the distribution function in phase space. Moreover, more realistic collision operator for Si takes into account the different equivalent valleys in the conduction band of Si leading to several optical-phonon scattering operators with different frequencies $\hbar\omega$ and optical coupling constants D_tk, see for instance [15] and the references therein. Finally, we will

show a comparison of our results in this case to multi-group WENO results as in [12]. This numerical scheme is based on the use of the cell average method for treating the dependence of the electron distribution function on the three-dimensional wave vector and a fifth-order WENO solver for dealing with the physical space variables.

2 Pointwise WENO time splitting scheme for the BP equation

Let us first reduce the BP system to dimensionless cartesian coordinates. We assume that the doping profile, the potential and thus the force field are only x-dependent in space and thus, our device spans over the x-direction. Let us use the following adimensionalization of the BP system:

adim.	parameter	400 nm device	50 nm device
$\tilde{k}=k^*k$	$k^*=\frac{\sqrt{2m^*k_bT_L}}{\hbar}$	$4.65974\times10^8 m^{-1}$	$4.65974\times10^8 m^{-1}$
$\tilde{x}=l^*x$	$l^*=$device length	$1\ \mu m$	$250\ nm$
$\tilde{t}=t^*t$	$t^*=$typical time	$1\ ps=10^{-12}s$	$1\ ps=10^{-12}s$
$\tilde{V}(\tilde{x})=V^*V(x)$	$V^*=$typical Vbias	$1V$	$1V$
$\tilde{E}(\tilde{x})=E^*E(x)$	$E^*=\frac{1}{10}\frac{V^*}{l^*}$	$100000Vm^{-1}$	$400000Vm^{-1}$
$\tilde{\varepsilon}(\tilde{k})=\varepsilon^*\varepsilon(k)$	$\epsilon^*=\frac{\hbar^2k^{*2}}{2m^*}$	$4.14195e-21$	$4.14195e-21$
$\tilde{\rho}(\tilde{x})=\rho^*\rho(x)$	$\rho^*=\left(\frac{2m^*k_BT_L}{\hbar}\right)^{3/2}$	1.01178×10^{26}	1.01178×10^{26}
$\tilde{j}(\tilde{x})=j^*j(x)$	$j^*=\frac{1}{l^{*2}t^*}$	10^{24}	1.6×10^{25}
$\tilde{u}(\tilde{x})=u^*u(x)$	$u^*=\frac{l^*}{t^*}$	10^6	250000
$\tilde{W}(\tilde{x})=W^*W(x)$	$W^*=(l^*/t^*)^2$	10^{12}	6.25×10^{10}

where tildes are written over dimensional magnitudes. Numerical values for all the parameters and the constants involved in the computations, as well as a resumé of all the dimensionless equations, can be found in the appendix. The BP equation transforms into

$$\frac{\partial f}{\partial t}+c_x\frac{\partial \varepsilon}{\partial k_1}\frac{\partial f}{\partial x}-c_kE_x\frac{\partial f}{\partial k_1}=\mathcal{Q}[f], \tag{2.1}$$

where the dimensionless parameters are

$$c_x=\frac{t^*\varepsilon^*}{\hbar k^*l^*},\qquad c_k=\frac{qt^*E^*}{\hbar k^*}.$$

The electrostatic field is self-consistently computed by the rescaled Poisson equation

$$\frac{\partial^2\Phi}{\partial x^2}=c_p[\rho(t,x)-N_D(x)],\qquad c_p=\frac{q\rho^*l^{*2}}{\epsilon\Phi^*},$$

coupled with appropriate boundary values ($\Phi(0)=0$, $\Phi(L)=$Vbias).

The advantage of conserving the cartesian structure is that, thanks to the time splitting techniques [7,23], we can apply the semi-lagrangian based Flux Balance Method [6,9] to

solve each transport step, which would be more involved in the energy-band adapted coordinates [4], the energy flux resulting to be energy-dependent. On the other hand, we have to deal with a more complicated computation of the collisional part: instead of being a simple evaluation, like in [4] we shall need to reconstruct the values of the probability density f along a circle in the k-dimension.

In order to integrate the collisional part, we use that f only depends on k_1 and $k_{23}=\|(k_2,k_3)\|=\sqrt{k_2^2+k_3^2}$, i.e., $f(k_1,k_2,k_3)=f(k_1,k_{23})$ due to symmetry considerations for this one-dimensional device. Using a change to polar coordinates in the (k_2,k_3)-plane, after straightforward computations, we obtain for the gain and the loss part of the collision operator $\mathcal{Q}(f)$ the following expressions:

$$\begin{aligned}\mathcal{Q}^+[f]=c_0\pi\int_{-\sqrt{\gamma_0(k)}}^{\sqrt{\gamma_0(k)}}f\left(k'_1,\sqrt{\gamma_0(k)-k'^2_1}\right)dk'_1+c_+\pi\int_{-\sqrt{\gamma_+(k)}}^{\sqrt{\gamma_+(k)}}f\left(k'_1,\sqrt{\gamma_+(k)-k'^2_1}\right)dk'_1\\ +\chi_{\{\gamma_-(k)>0\}}c_-\pi\int_{-\sqrt{\gamma_-(k)}}^{\sqrt{\gamma_-(k)}}f\left(k'_1,\sqrt{\gamma_-(k)-k'^2_1}\right)dk'_1,\end{aligned}\tag{2.2}$$

with $\gamma_0(k)=\varepsilon(k)$, $\gamma_+(k)=\varepsilon(k)+h\omega/\varepsilon^*$, $\gamma_-(k)=\varepsilon(k)-\hbar\omega/\varepsilon^*$, and

$$\mathcal{Q}^-[f]=c_0 2\pi\sqrt{\gamma_0(k)}f(k)+\chi_{\{\gamma_-(k)>0\}}c_+2\pi\sqrt{\gamma_-(k)}f(k)+c_-2\pi\sqrt{\gamma_+(k)}f(k),$$

with the dimensionless parameters

$$c_0=\frac{K_0t^*k^{*3}}{\varepsilon^*},\qquad c_+=\frac{Kt^*(n_q+1)k^{*3}}{\varepsilon^*},\qquad c_-=\frac{Kt^*n_qk^{*3}}{\varepsilon^*}.$$

In the next subsections, we shall explain in detail both the transport and the collision steps in this method. Let us finally comment that Poisson's equation is solved through a standard centered finite differences leading to solving a linear system with a tridiagonal matrix.

2.1 Numerical scheme

Eq. (2.1) is solved through a time splitting scheme dividing the system into the solution of transport steps and collision steps being the time stepping fixed. The computational domain is discretized into a tensor product mesh, and a uniform mesh is taken in each direction: $t_n=n\Delta t$, and

$$\begin{aligned}&x_i=i\Delta x, && i=0,\cdots,N_x-1, && \Delta x=\tfrac{1}{N_x-1},\\ &(k_1)_j=-\varepsilon^{-1}(\alpha\bar{N})+j\Delta k_1, && j=0,\cdots,N_{k_1}-1, && \Delta k_1=\tfrac{2\varepsilon^{-1}(\alpha\bar{N})}{N_{k_1}-1},\\ &(k_{23})_k=k\Delta k_{23}, && k=0,\cdots,N_{k_{23}}-1, && \Delta k_{23}=\tfrac{\varepsilon^{-1}(\alpha\bar{N})}{N_{k_{23}}-1},\end{aligned}$$

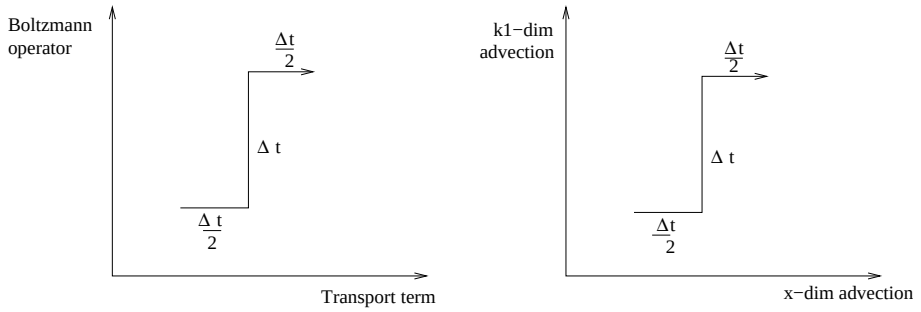

Figure 1: Time splitting scheme, see Appendix (Subsection A.2) for a fully detailed splitting scheme.

where α is the dimensionless energy $\alpha=\hbar\omega/k_BT_L$. Here, $\bar{N}$ is an integer chosen as a maximal bound for the adimensionalized energy-band function

$$\varepsilon(k)=(k_1)^2+(k_2)^2+(k_3)^2=(k_1)^2+(k_{23})^2=\varepsilon[k_1,k_{23}].$$

More precisely, at the value $\bar{N}\alpha$

$$\varepsilon\left[(k_1)_{N_{k_1}-1},0\right]=\bar{N}\alpha,\qquad \varepsilon\left[0,(k_{23})_{N_{k_{23}}-1}\right]=\bar{N}\alpha,$$

a magnitude which is related to the resolution in the (k_1,k_{23})-space.

The approximation denoted by $f^n_{i,j,k}$ to the point values of $f\left(t_n,x_i,(k_1)_j,(k_{23})_k\right)$ are obtained through the second order time splitting scheme [7] subdividing the BP system (2.1):

- **Step 1.** Solve $\dfrac{\partial f}{\partial t}+c_x\dfrac{\partial\varepsilon}{\partial k_1}\dfrac{\partial f}{\partial x}-c_kE_x\dfrac{\partial f}{\partial k_1}=0$ for a $\Delta t/2$-time step;
- **Step 2.** Solve $\dfrac{\partial f}{\partial t}=\mathcal{Q}[f]$ for a Δt-time step;
- **Step 3.** Solve $\dfrac{\partial f}{\partial t}+c_x\dfrac{\partial\varepsilon}{\partial k_1}\dfrac{\partial f}{\partial x}-c_kE_x\dfrac{\partial f}{\partial k_1}=0$ for a $\Delta t/2$-time step.

The same procedure is used for solving the two transport steps

$$\frac{\partial f}{\partial t}+c_x\frac{\partial\varepsilon}{\partial k_1}\frac{\partial f}{\partial x}-c_kE_x\frac{\partial f}{\partial k_1}=0$$

by dimensional splitting. Therefore, we have subdivided the problem into the solution of the x-transport, the k-transport and the collision:

$$\frac{\partial f}{\partial t}+\underbrace{\overbrace{c_x\frac{\partial\varepsilon}{\partial k_1}\frac{\partial f}{\partial x}}^{x\text{-transport}}-\overbrace{c_kE_x\frac{\partial f}{\partial k_1}}^{k\text{-transport}}}_{\text{transport}}=\underbrace{\mathcal{Q}[f]}_{\text{collisions}}$$

as sketched in Fig. 1 and fully specified in the Appendix (Subsection A.2).

Remark 2.1 (Time Splittings)**.** In principle, the above time splitting procedure (TS) may seem unnecessary complicated due to the splitting of three different operators. Actually, the use of a direct first-order splitting, as reminded to the reader in Subsection A.3, would seem appropriate for simplicity. In Section 3 we will compare the results for both splitting algorithms, and we will show that results given by the above splitting procedure improve the ones given by the first-order splitting.

Numerical scheme: transport step

Each transport block is solved by the Flux Balance Method [6, 9]: when solving the x-transport, k_1 and k_{23} act as parameters, as well as x and k_{23} when solving the k_1-transport. This method is based on the semi-lagrangian approach of following the characteristics backwards; the improvement is that we force the mass conservation, unlike the direct method, which gives no guarantee about this point. The solution of the x-transport gives

$$f^{**}_{i,j,k}=f^{*}_{i,j,k}+\frac{1}{\Delta x}\{[F(x_{i-1/2})-F(x_{i-1/2}-c_x\nabla_k\varepsilon\Delta t)] - [F(x_{i+1/2})-F(x_{i+1/2}-c_x\nabla_k\varepsilon\Delta t)]\}, \quad F(x)=\int_0^x f^*\left[\xi,(k_1)_j,(k_{23})_k\right]d\xi,$$

and, as for the solution of the k_1-transport,

$$f^{**}_{i,j,k}=f^{*}_{i,j,k}+\frac{1}{\Delta k_1}\left\{\left[F((k_1)_{j-1/2})-F((k_1)_{j-1/2}+c_kE\Delta t)\right] - [F((k_1)_{i+1/2})-F((k_1)_{i+1/2}+c_kE\Delta t)]\right\}, \quad F(k_1)=\int_0^{k_1} f^*[x_i,\xi,(k_{23})_k]d\xi.$$

More details about the FBM method can be found in [6,9]. In order to compute the fluxes, for instance,

$$F(x_{i+1/2})-F(x_{i+1/2}-c_x\nabla_k\varepsilon),$$

we reconstruct the values $F(x_{i+1/2}-c_x\nabla_k\varepsilon)$, given the known values of the primitive at the grid points $F(x_{i+1/2})$, by the fifth order Pointwise WENO-6,4 interpolation summarized in next subsection.

Numerical scheme: collision step

In order to solve the collision step, we need to compute some integrals along semicircles of radius $\gamma_0(k)$, $\gamma_+(k)$ and $\gamma_-(k)$ in the (k_1,k_{23})-space. Fig. 2 explains two different ways in which we can perform it. We may first use a direct linear interpolation between the closest points in the cartesian grid as specified in Fig. 2 (left). The integration rule to compute the final approximation of (2.2) is coherently chosen in terms of accuracy as the trapezoidal rule.

On the other hand, we can choose a WENO-4,3 interpolation along the $k_1=(k_1)_j$ line where the point lies as in Fig. 2 (right). This interpolation is performed on the stencil $((k_1)_j,(k_{23})_{l-1}),\cdots,((k_1)_j,(k_{23})_{l+2})$. If not enough points are available (i.e., $l=0$

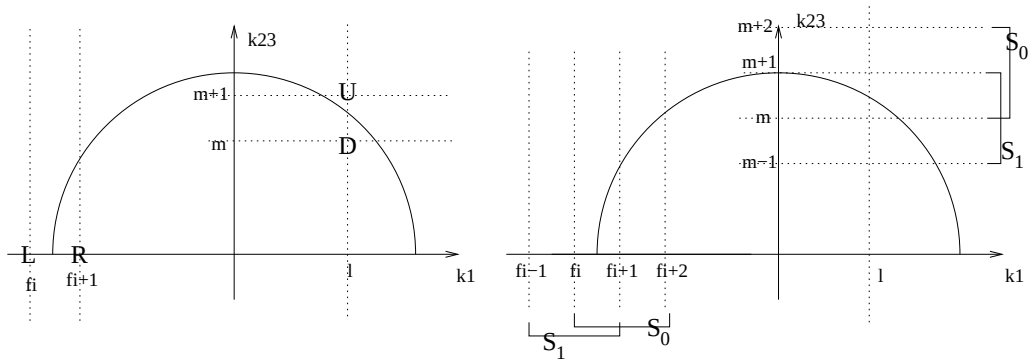

Figure 2: The integration on the interval $[-\sqrt{\gamma},\sqrt{\gamma}]$. Left: the needed values are obtained through a linear interpolation on the two closest points lying either on the $k_{23}=0$ line (for the first and last point) or on the $k_1=l$ line (for the other points). Right: the needed values are obtained through PWENO-4,3 interpolation on the closest points lying either on the $k_{23}=0$ line (for the first and last point) or on the $k_1=l$ line (for the other points).

or $l \geq N_{k_{23}}-2$), we use Lagrange-3 on the proper stencil. Consistently with a degree-2 polynomial interpolation, as integration rule for (2.2), we choose Simpson's rule. This WENO-4,3 interpolation procedure will be detailed in next subsection. A similar interpolation procedure was used in [21] to cope with analogous problems in a computational fluid dynamics problem.

We can now explain the implemented boundary conditions:

- at $x=0$ and $x=L$ we use the following inflow/outflow condition:

$$f^n_{-i,j,k}=\begin{cases} f^n_{0,j,k}, & k_1<0, \\ \dfrac{N_D(0)}{\rho(0)} f^n_{0,j,k}, & k_1\geq 0, \end{cases}$$

  and

$$f^n_{N_x-1+i,j,k}=\begin{cases} f^n_{N_x-1,j,k}, & k_1>0, \\ \dfrac{N_D(L)}{\rho(L)} f^n_{N_x-1,j,k}, & k_1\leq 0, \end{cases}$$

  in order to have the ghost points we need for the PWENO interpolation and to preserve the correct values of the distribution function at the drain and the source of the diode;

- at $k_1=-\varepsilon^{-1}(\alpha\bar{N})$ and $k_1=\varepsilon^{-1}(\alpha\bar{N})$ a Neumann type boundary condition in used:

$$f^n_{i,-j,k}=f^n_{i,0,k} \qquad \text{and} \qquad f^n_{i,N_{k_1}-1+j,k}=f^n_{i,N_{k_1}-1,k}.$$

While in the transport steps the mass conservation is guaranteed by the Flux Balance Method being conservative, during the collision steps we numerically impose the mass

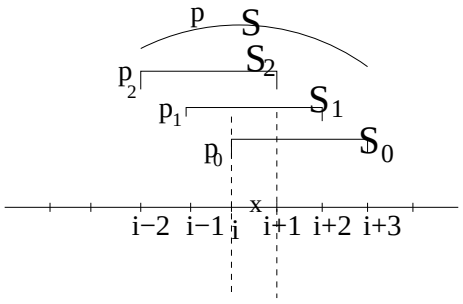

Figure 3: WENO-6,4 interpolation: the stencil $\mathcal{S}_r$ corresponds to the points interpolated by the 3-degree Lagrange polynomial $p_r(x)$. The whole stencil $\mathcal{S}=\cup_{r=0}^{2}\mathcal{S}_r$ is interpolated by the 5-degree Lagrange polynomial $p(x)$. The smoothness indicators β_r depend on the derivatives of $p_r(x)$ in the central interval (x_i,x_{i+1}) (between the dashed lines).

conservation by redefining the collision operator by

$$\mathcal{Q}[f]=\mathcal{Q}^+[f]-\frac{\int_{\mathbb{R}^3}\mathcal{Q}^+[f]dk}{\int_{\mathbb{R}^3}\mathcal{Q}^-[f]dk}\mathcal{Q}^-[f].$$

2.2 PWENO-6,4 interpolation

PWENO (Pointwise Weighted Essentially Non Oscillatory) methods have been developed [6] in order to compute a direct interpolation (i.e. we want to reconstruct the values of the very function, we do not want values by which we reconstruct high-order derivatives, like in the case of WENO methods for finite differences [14, 22]) which avoids Lagrange spurious oscillations produced where high derivatives appear. Here we just introduce WENO-6,4 method (its order is 5), a centered interpolation based on a six points stencil.

PWENO-6,4 interpolation is a convex combination by $\{\omega_r(x)\}_{r=0,1,2}$ of the reconstruction given by three Lagrange polynomials $\{p_r(x)\}_{r=0,1,2}$:

$$p^W(x)=\omega_0(x)p_0(x)+\omega_1(x)p_1(x)+\omega_2(x)p_2(x),$$

like we see in Fig. 3. We wish to obtain a non-oscillatory reconstruction when the function to be interpolated is "irregular", i.e. when high gradients appear. Once we have a measurement of its regularity by the smoothness indicators $\{\beta_r\}_{r=0,1,2}$, we shall need to define other weights $\{d_r(x)\}_{r=0,1,2}$ in order to push the interpolation to the highest order in the case of a smooth function, i.e. in order to rescue a Lagrange-like behavior, which is order 6, the highest. Weights ω_r are the normalization (by $\omega_0(x)+\omega_1(x)+\omega_2(x)=1$) of the protoweights

$$\tilde{\omega}_r(x)=\frac{d_r(x)}{(\epsilon+\beta_r)^p},\qquad \epsilon \text{ small and positive, in the code } \epsilon=10^{-6}. \tag{2.3}$$

The positive parameter ϵ is needed in order to avoid the denominator to be zero, and it must be small so as not to perturb the desired behavior of the weights. In the literature $\epsilon = 10^{-6}$, because it is reasonable for numerical computing. Exponent p is set $p=2$; changing it means modifying the relative presence of the regular and irregular stencils.

We can now define "irregular" a function whose β_r are different orders, and "regular" a function whose β_r are same order. Remark that if $\beta_0=\beta_1=\beta_2$ then $\omega_r(x)=d_r(x)$, i.e. we would obtain exactly the highest order Lagrange interpolation, as it will be made clear later on by equation (2.4).

The following smoothness measurement was proposed by Jiang and Shu in [14]:

$$\beta_r=\sum_{l=1}^{3}\Delta x^{2l-1}\left\|\frac{d^l}{dx^l}p_r\right\|^2_{L^2(x_i,x_{i+1})} \qquad \text{for } r=0,1,2.$$

This is a sort of Sobolev norm, where the weights Δx^{2l-1} are needed to make all the terms of the sum independent of Δx, i.e., to make them all be of the same order. After straightforward calculations, we have

$$\begin{cases} \beta_0=\frac{248}{15}f_{i+2}^2-\frac{2309}{60}f_{i+1}f_{i+2}+\frac{439}{30}f_if_{i+2}-\frac{553}{60}f_{i+2}f_{i+3}+\frac{721}{30}f_{i+1}^2 \\ \quad -\frac{1193}{60}f_if_{i+1}+\frac{103}{10}f_{i+1}f_{i+3}+\frac{407}{90}f_i^2-\frac{683}{180}f_if_{i+3}+\frac{61}{45}f_{i+3}^2, \\ \beta_1=\frac{61}{45}f_{i+2}^2+\frac{61}{45}f_{i-1}^2+\frac{179}{30}f_{i-1}f_{i+1}-\frac{141}{20}f_{i-1}f_i-\frac{293}{180}f_{i-1}f_{i+2} \\ \quad -\frac{141}{20}f_{i+1}f_{i+2}+\frac{179}{30}f_if_{i+2}+\frac{331}{30}f_{i+1}^2-\frac{1259}{60}f_if_{i+1}+\frac{331}{30}f_i^2, \\ \beta_2=\frac{248}{15}f_{i-1}^2+\frac{439}{30}f_{i-1}f_{i+2}-\frac{2309}{60}f_{i-1}f_i+\frac{407}{90}f_{i+1}^2-\frac{1193}{60}f_if_{i+1} \\ \quad +\frac{721}{30}f_i^2+\frac{103}{10}f_{i-2}f_i-\frac{553}{60}f_{i-2}f_{i-1}+\frac{61}{45}f_{i-2}^2-\frac{683}{180}f_{i-2}f_{i+1}. \end{cases}$$

In order to achieve a high-order reconstruction for regular functions, we define coefficients $d_r(x)$ this way:

$$p(x)=\sum_{r=0}^{2}d_r(x)p_r(x), \tag{2.4}$$

where $p(x)$ is the 6th-order Lagrange polynomial interpolating the whole stencil $\mathcal{S}$ (see Fig. 3). After straightforward calculations, we have

$$\begin{cases} d_0(x)=\frac{1}{20\Delta x^2}(x-x_{i-1})(x-x_{i-2}), \\ d_1(x)=-\frac{1}{20\Delta x^2}((x-x_{i-2})(x-x_{i+3})+(x-x_{i+3})(x-x_{i-2})), \\ d_2(x)=\frac{1}{20\Delta x^2}(x-x_{i+2})(x-x_{i+3}). \end{cases}$$

Remark 2.2 (PWENO-4,3 interpolation)**.** We give here the parameters to perform the PWENO-4,3 interpolation, which is based exactly on the same ideas of PWENO-6,4 interpolation, the difference being that instead of three stencils made of four points each, we use two stencils made of three points each. The Lagrange polynomials are

$$\begin{cases} p_0(x)=\dfrac{(x-x_{i+1})(x-x_{i+2})}{2\Delta x^2}f_i-\dfrac{(x-x_i)(x-x_{i+2})}{\Delta x^2}f_{i+1}+\dfrac{(x-x_i)(x-x_{i+1})}{2\Delta x^2}f_{i+2}, \\ p_1(x)=\dfrac{(x-x_i)(x-x_{i+1})}{2\Delta x^2}f_{i-1}-\dfrac{(x-x_{i-1})(x-x_{i+1})}{\Delta x^2}f_i+\dfrac{(x-x_{i-1})(x-x_i)}{2\Delta x^2}f_{i+1}, \end{cases}$$

the weights $d_r(x)$ are

$$d_0(x)=\frac{x-x_{i-1}}{3\Delta x}, \qquad d_1(x)=-\frac{x-x_{i+2}}{3\Delta x},$$

and the smoothness indicators are

$$\begin{cases} \beta_0=\dfrac{25}{12}f_i^2+\dfrac{16}{3}f_{i+1}^2+\dfrac{13}{12}f_{i+2}^2+\dfrac{13}{12}f_if_{i+2}-\dfrac{13}{3}f_{i+1}f_{i+2}-\dfrac{19}{3}f_if_{i+1}, \\ \beta_1=\dfrac{16}{3}f_i^2+\dfrac{25}{12}f_{i+1}^2+\dfrac{13}{12}f_{i-1}^2-\dfrac{13}{3}f_{i-1}f_i+\dfrac{13}{6}f_{i-1}f_{i+1}-\dfrac{19}{3}f_if_{i+1}. \end{cases}$$

3 Numerical experiments

3.1 Steady-state results for the diodes

We consider two test examples: Si n^+-n-n^+ diodes of total length of $1\mu m$ and $0.25\mu m$, with $400nm$ and $50nm$ channels located in the middle of the device respectively. For the $400nm$ device and the $50nm$ device the dimensional doping is, respectively,

$$N_D=\begin{cases} 5\times10^{17}\ cm^{-3} & n^+\text{-zone} \\ 2\times10^{15}\ cm^{-3} & n\text{-zone} \end{cases} \text{ and } \begin{cases} 5\times10^{18}\ cm^{-3} & n^+\text{-zone}, \\ 1\times10^{15}\ cm^{-3} & n\text{-zone}. \end{cases}$$

The results provided by the W5FD method [4] and our PW5TS are compared as for the macroscopic magnitudes (density, electrostatic potential, electrostatic field, mean velocity, energy and current), as we can see in Figs. 4 to 10. In the W5FD scheme the kinetic variable ω denotes the dimensionless electron energy and μ the cosine of the angle between the wave vector k and the x-axis.

The comparisons are set in such a way that we can infer how the choice of the different parameters of our scheme affects the results compared to the W5FD results chosen as benchmarks. Five issues have been considered: the order of the time splitting procedure, the energy cut-off $\bar{N}$, the type of interpolation chosen for computing the collision operator, the resolution in k and the time step Δt. Detailed comparisons of these parameters are shown for the 400 nm diode, whereas certain comparisons are drawn for the 50 nm diode.

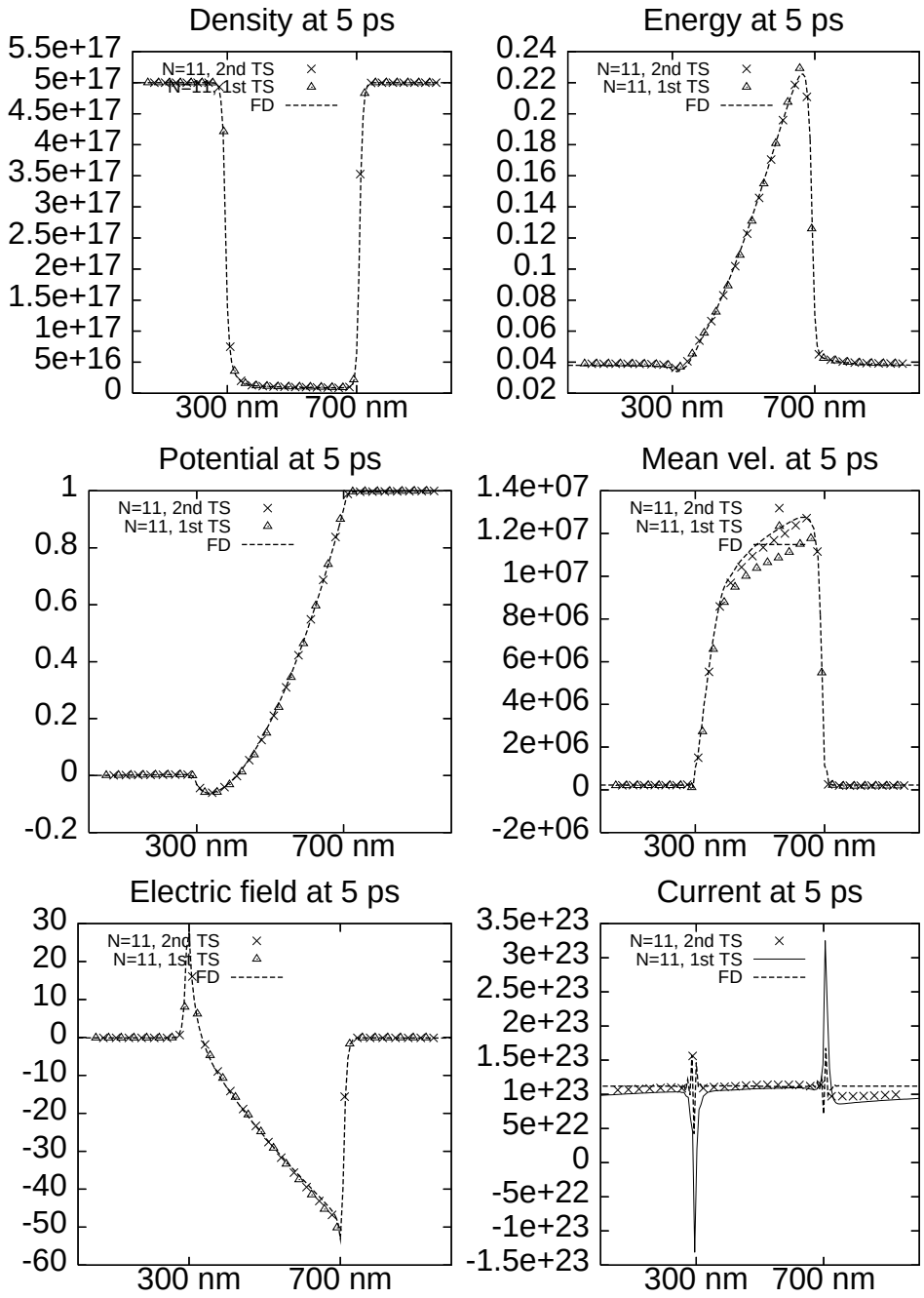

Figure 4: Comparison between some macroscopic quantities of the 400 nm diode at equilibrium (5 ps) given by splitting schemes of order 1 and 2. Top left: density in cm^{-3}; top right: energy in eV; center left: potential in V; center right: mean velocity in $cm\ s^{-1}$; bottom left: electric field in $10^3 V/cm$; bottom right: current in $cm^{-2}s^{-1}$. Grids are set $150\times40\times16$ for (x,ω,μ) for the W5FD method, $150\times71\times71$ for $(x,k_1,k_{23}=\|(k_2,k_3)\|)$, $\bar{N}=11$, $\Delta t=0.01ps$, linear interpolation for collisions, for the PW5TS method.

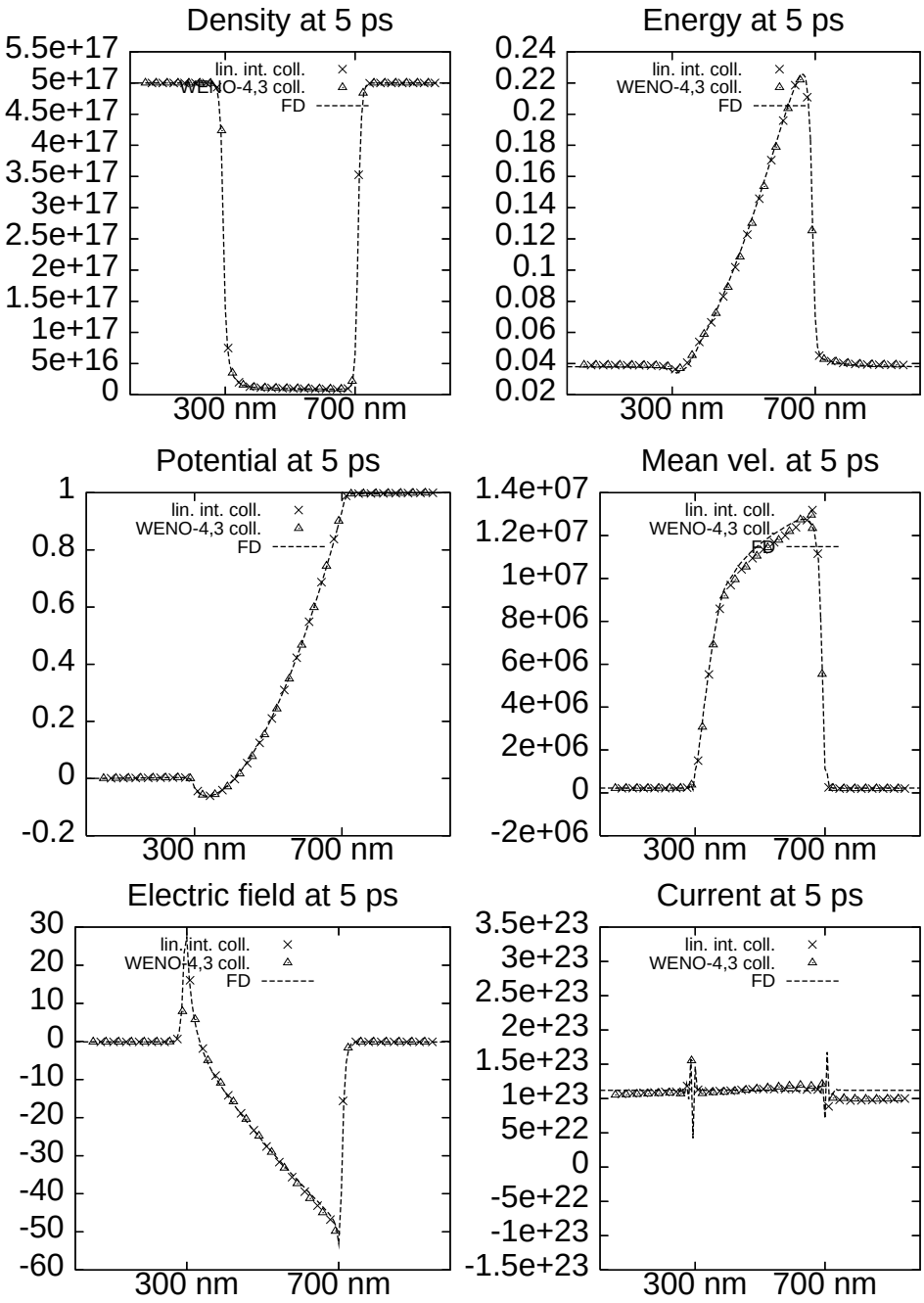

Figure 5: Comparison between some macroscopic quantities of the 400 nm diode at equilibrium (5 ps) given by different integrations of the collisions, wither by linear interpolation or by PWENO-4,3 interpolation. Top left: density in cm^{-3}; top right: energy in eV; center left: potential in V; center right: mean velocity in $cm\ s^{-1}$; bottom left: electric field in $10^3 V/cm$; bottom right: current in $cm^{-2}s^{-1}$. Grids are set $150\times40\times16$ for (x,ω,μ) for the W5FD method, $150\times71\times71$ for $(x,k_1,k_{23}=\|(k_2,k_3)\|)$, $\bar{N}=11$, $\Delta t=0.01ps$, 2nd order TS, for the PW5TS method.

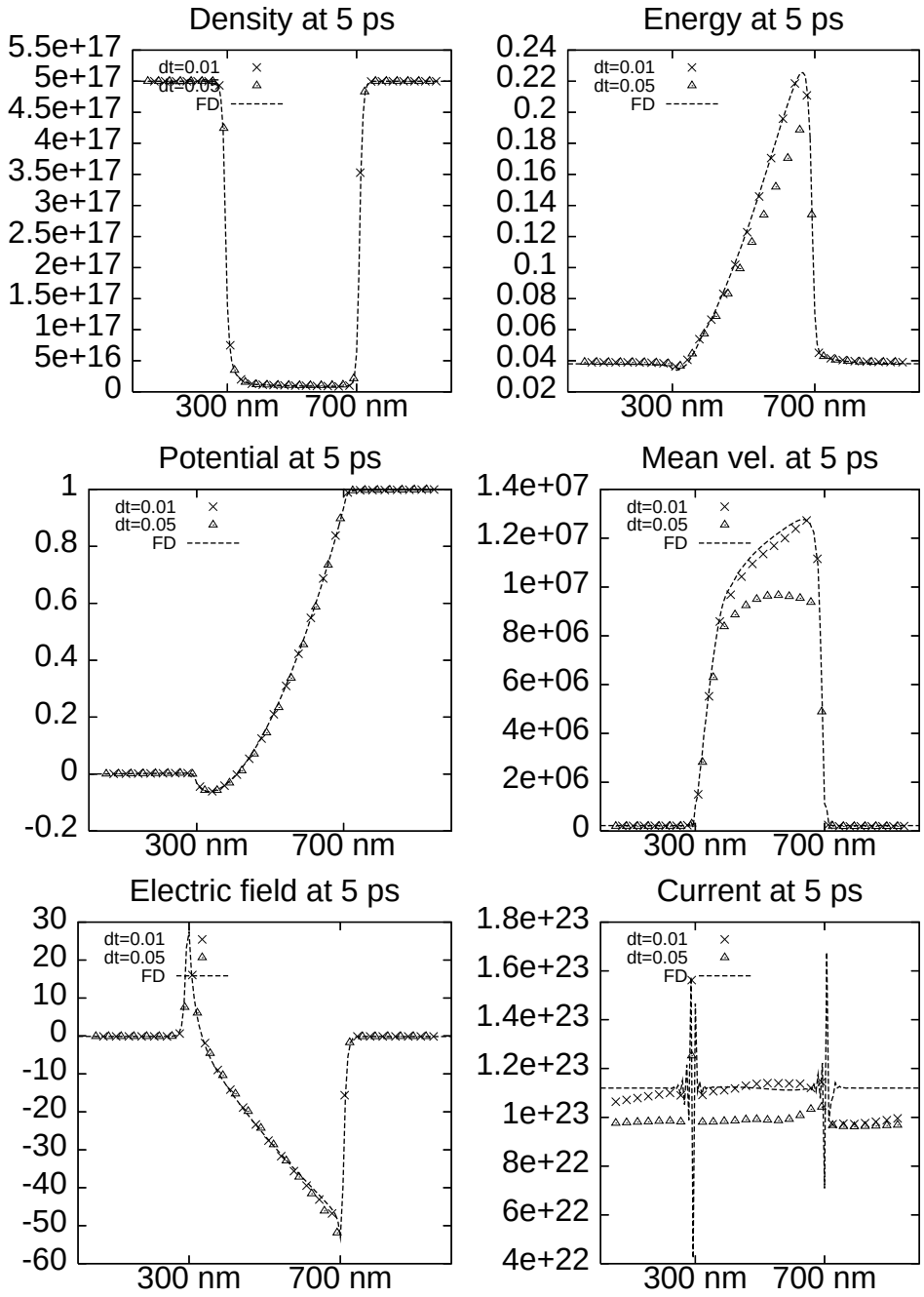

Figure 6: Comparison between some macroscopic quantities of the 400 nm diode at equilibrium (5 ps) given by different time steppings. Top left: density in cm^{-3}; top right: energy in eV; center left: potential in V; center right: mean velocity in $cm\ s^{-1}$; bottom left: electric field in $10^3 V/cm$; bottom right: current in $cm^{-2}s^{-1}$. Grids are set $150\times40\times16$ for (x,ω,μ) for the W5FD method, $150\times71\times71$ for $(x,k_1,k_{23}=\|(k_2,k_3)\|)$, $\bar{N}=11$, linear interpolation for collisions, 2nd order TS, for the PW5TS method.

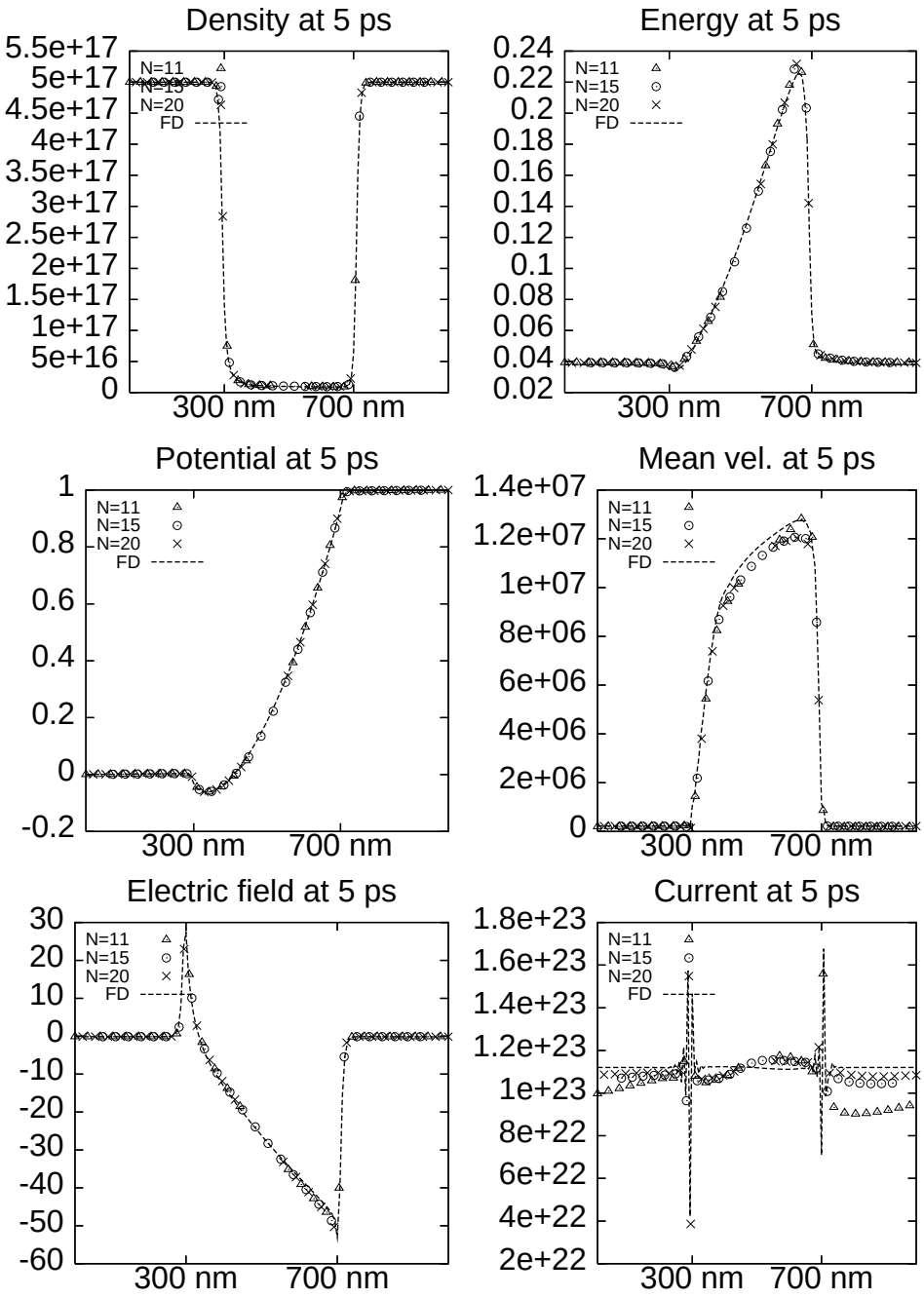

Figure 7: Comparison between some macroscopic quantities of the 400 nm diode at equilibrium (5 ps) given by different $\bar{N}$. Top left: density in cm^{-3}; top right: energy in eV; center left: potential in V; center right: mean velocity in $cm\ s^{-1}$; bottom left: electric field in $10^3 V/cm$; bottom right: current in $cm^{-2}s^{-1}$. Grids are set $150\times40\times16$ for (x,ω,μ) for the W5FD method, $150\times64\times64$ for $(x,k_1,k_{23}=\|(k_2,k_3)\|)$ (when $\bar{N}=10$), $\Delta t=0.01ps$, linear interpolation for collisions, 2nd order TS, for the PW5TS method.

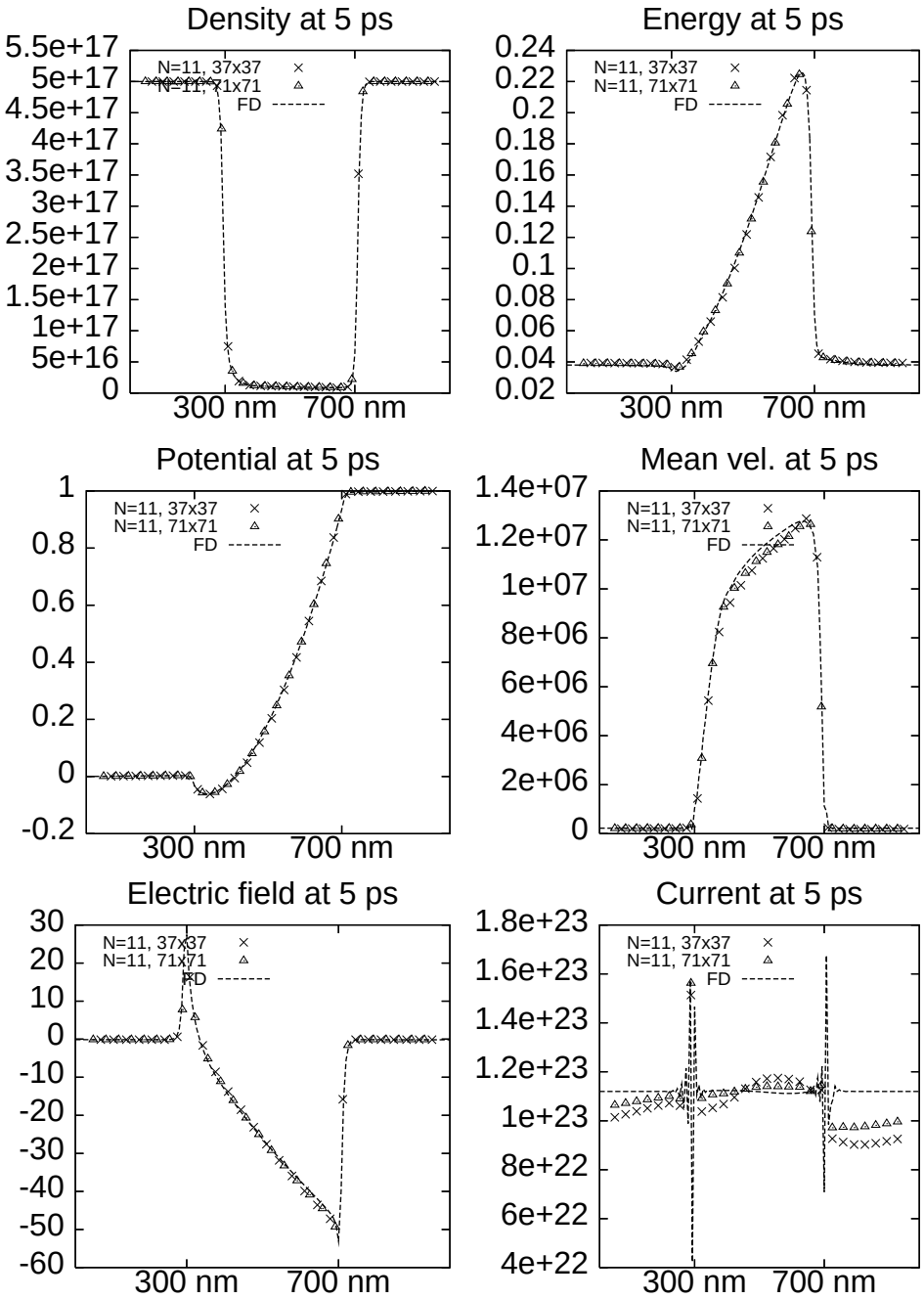

Figure 8: Comparison between some macroscopic quantities of the 400 nm diode at equilibrium (5 ps) given by different resolutions of the (k_1,k_{23})-grid. Top left: density in cm^{-3}; top right: energy in eV; center left: potential in V; center right: mean velocity in $cm\ s^{-1}$; bottom left: electric field in $10^3 V/cm$; bottom right: current in $cm^{-2}s^{-1}$. Grids are set $150\times40\times16$ for (x,ω,μ) for the W5FD method, $\bar{N}=11$, $\Delta t=0.01ps$, linear interpolation for collisions, 2nd order TS, for the PW5TS method.

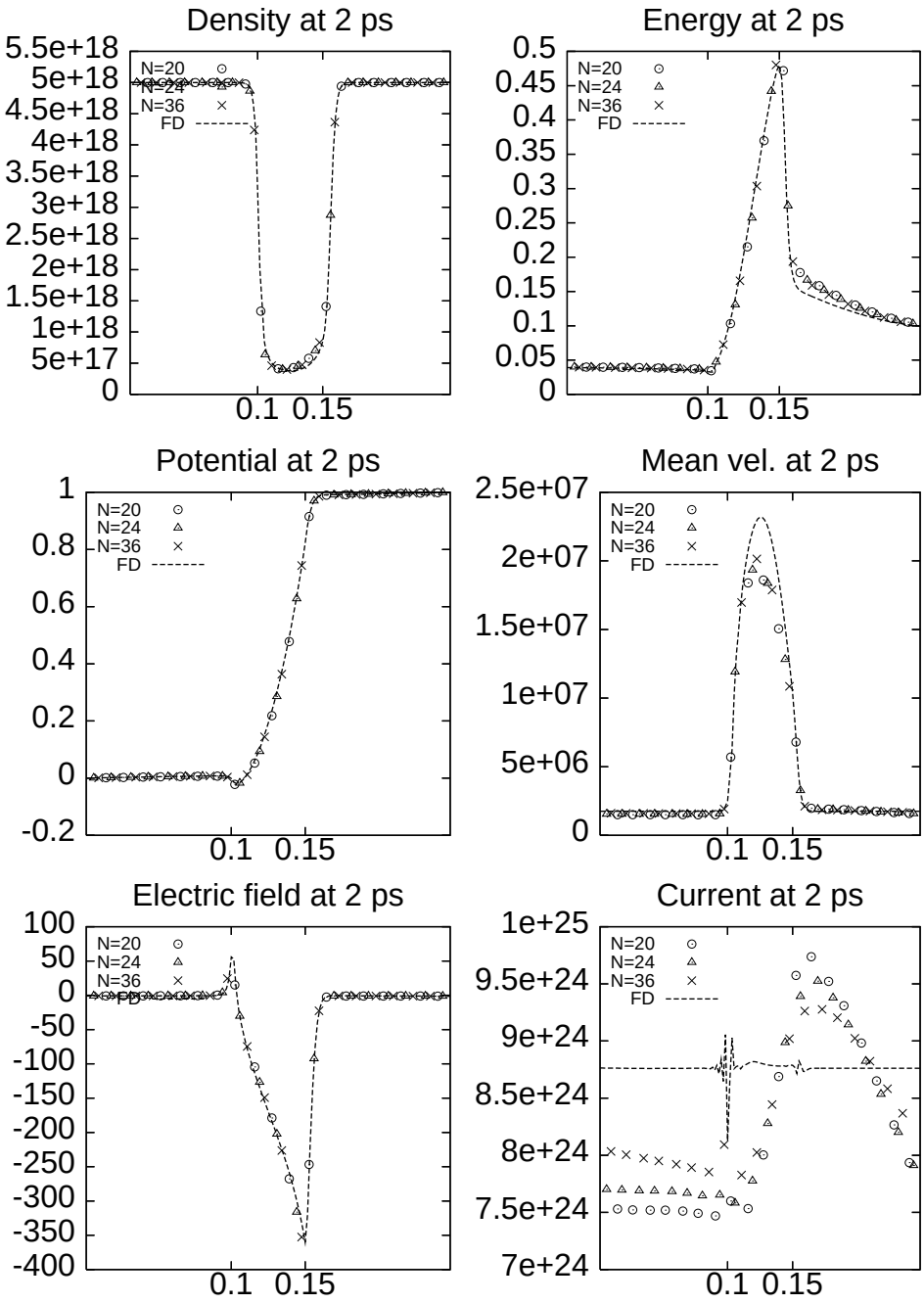

Figure 9: Comparison between some macroscopic quantities of the 50 nm diode at equilibrium (2 ps) given by different $\bar{N}$. Top left: density in cm^{-3}; center left: potential in V; top right: energy in eV; center right: mean velocity in $cm\ s^{-1}$; bottom left: electric field in $10^3 V/cm$; bottom right: current in $cm^{-2}s^{-1}$. Grids are set $150\times144\times16$ for (x,ω,μ) for the W5FD method, $150\times32\times32$ for $(x,k_1,k_{23}=\|(k_2,k_3)\|)$ (when $\bar{N}=18$), $\Delta t=0.01ps$, linear interpolation for the collisions, 2nd order TS, for the PW5TS method.

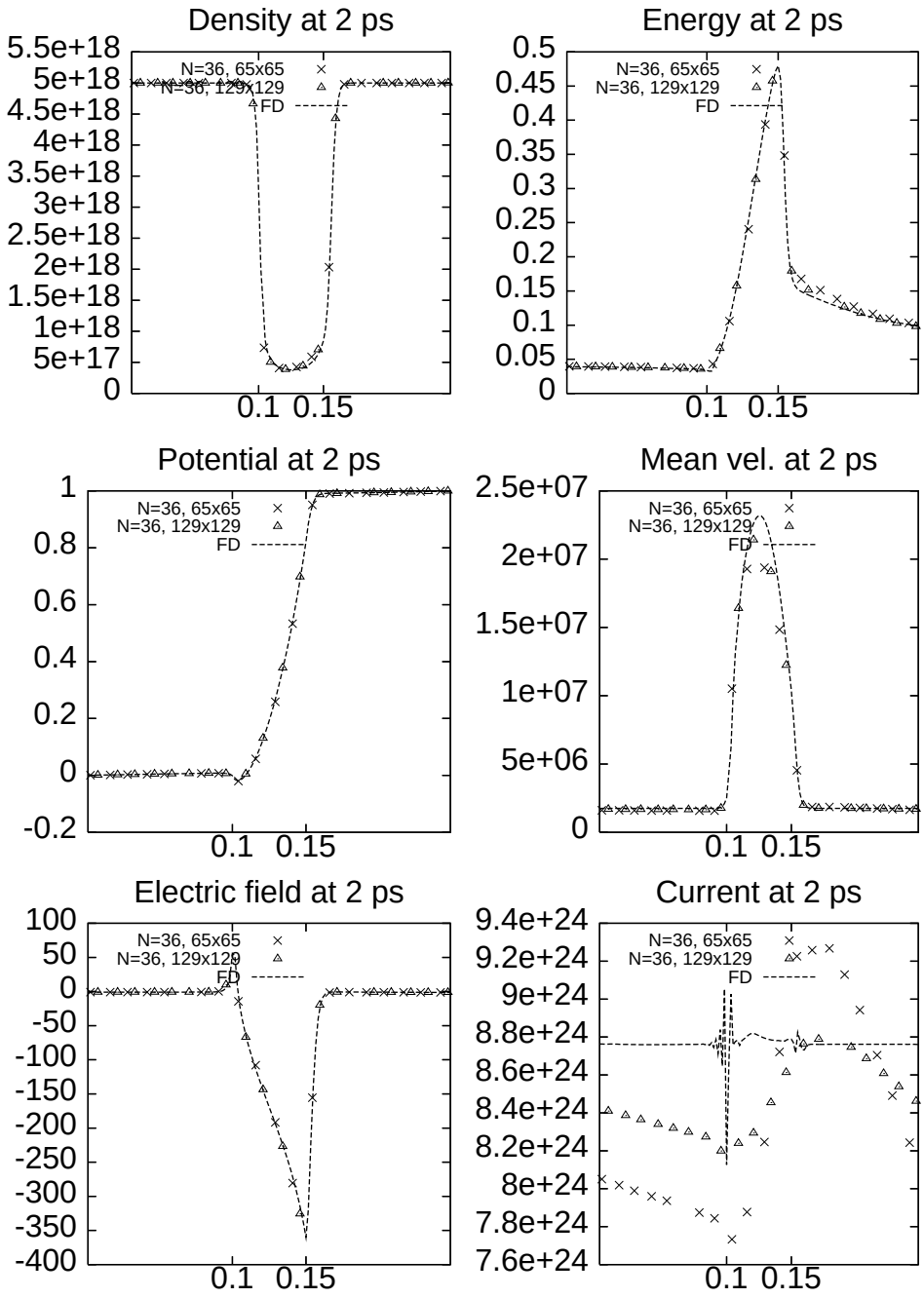

Figure 10: Comparison between some macroscopic quantities of the 50 nm diode at equilibrium (2 ps) given by different resolutions of the (k_1,k_{23})-grid. The grid is set $150\times144\times16$ for (x,ω,μ) for the W5FD method. $\bar{N}=20$, $\Delta t=0.01ps$, linear interpolation for the collisions, 2nd order TS, for the PW5TS method.

One advantage of the proposed method is that we have no restriction for the time stepping, thus in both cases we can reach the equilibrium (5 *ps* for the 400 *nm* diode, 2 *ps* for the 50 *nm* diode) by largely less time-steps than those in [4], where several thousands were needed. We have empirically searched for the largest time steppings by which no instabilities appear; for the 400 nm diode it seems to be around $\Delta t = 0.07$ *ps* (so by just about 70 steps we reach the equilibrium), for the 50 nm diode around $\Delta t = 0.04$ *ps*. As for the Finite Differences scheme, the adaptive time stepping situates between 10^{-3} and 10^{-4} *ps*.

The choice of shorter time steppings and better resolution in k due to finer grids or larger cut-off energy $\bar{N}$ improves the quality of the results, see Figs. 6 to 10; of course, the counterpart is that it increases the computational cost. The loss of reliability is evident when we increase the time stepping of the code if we look at the current and the mean velocity in Fig. 6, where the oscillations are amplified, even if the density, the electric potential and the electric field remain very close. Thus, unfortunately the improvement in the time stepping does not always translate into a shorter computational time, a better resolution in the k-dimension with larger grids and better adapted cut-off energy $\bar{N}$ being needed in order to obtain reliable results.

All the above results have been obtained by using the direct linear interpolation for the collisional step and the time splitting procedure in Subsection 2.1. Let us comment on this choice: we have tested and compared the direct linear interpolation and the PWENO-4,3 interpolations as discussed in Subsection 2.1 together with the first-order splitting and the TS splitting procedure in Subsection 2.1. In Figs. 4 and 5 results are compared in terms of the current and the mean velocity at equilibrium. We first observe that first-order splitting results are in general worse than the results with time splitting procedure in Subsection 2.1 and Appendix A.2. On the other hand, we observe that improving the accuracy of the interpolation procedure in the collision step from linear to PWENO-4,3 does not result in a marked gain of accuracy for these quantities. Even if results are not shown here, a simple two-dimensional linear, in each variable not jointly, interpolation in each quadrangle of the cartesian grid has been performed. Again, this improvement in the interpolation accuracy does not yield a significant gain in the accuracy of the macroscopic quantities. This collisional step will need further improvements or alternative methods as spectral approaches [8] before being able to cope with two dimensional devices in comparison to the efficiency of W5FD [5].

On the other hand, having a finer grid in the k-dimension, moreover in cartesian coordinates, permits a better resolution of the distribution function, as we can observe in Figs. 11 and 12: like in [4], the pdf outside the channel is close to a Maxwellian distribution. Inside the channel it looks like a shifted Maxwellian in the large diode, while in the small one it assumes a very asymmetric shape. Moreover, in this small diode we observe the formation of a narrow ballistic pick. A good resolution of this narrow pick involves a very fine grid in k-space and a much larger computational cost. Its underresolution is the cause of the difference and oscillations in mean velocity and current between the W5FD method [4] and our PW5TS observed in Fig. 10. Therefore, an energy-based variables

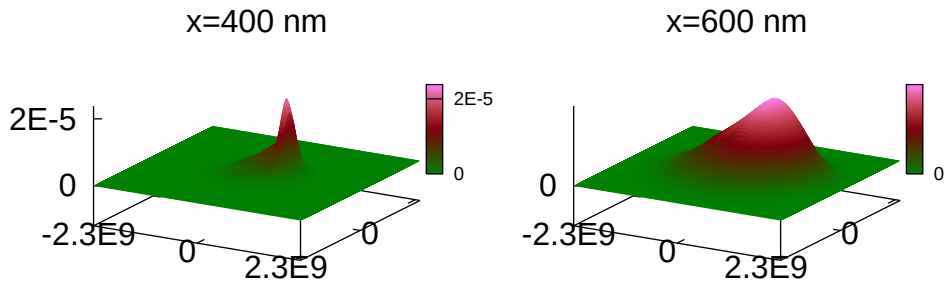

Figure 11: Distribution function of the 400 nm diode at time 5 ps given by the PW5TS method at different points of the device, for a $150\times71\times71$ grid, $\bar{N}=11$, $\Delta t=0.01ps$, 2nd order TS, linear interpolation for collisions.

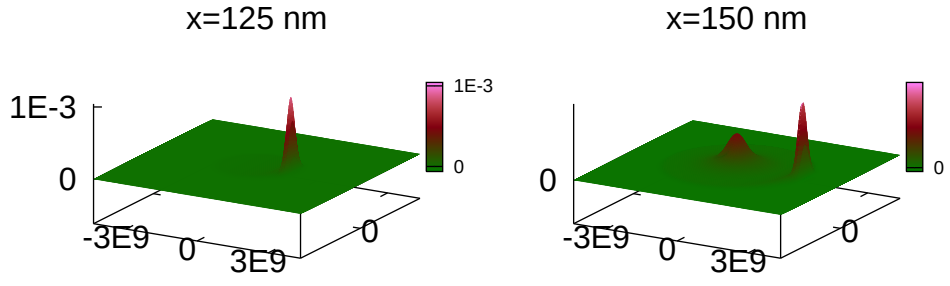

Figure 12: Distribution function of the 50 nm diode at time 2 ps given by the PW5TS method at different points of the device, for a $150\times129\times129$ grid, $\bar{N}=36$, $\Delta t=0.01ps$, 2nd order TS, linear interpolation for collisions.

solver as the one in [4] gives better results in this case.

Finally, let us point out that previous results have been obtained looking at the stabilization in time of the macroscopic quantities. For instance, in the 400-nm diode case, runs have been performed till 5ps for which the density is stabilized up to 10^{-6}. A stabilization of the other macroscopic quantities: current, mean velocity and energy needs longer runs till 10ps approx. Typical problems in reaching numerical steady states occur for splitting in time numerical strategies. In our case, the main issue is that the results stabilize numerically to states in which the current is not constant as it should be for the stationary case. We can observe this problem in the current comparison of Figs. 8 and 10. An improvement in the numerical approximation of the collisional step will certainly help to fix this problem.

3.2 Steady-state results in multifrequency phonons

With the method we have implemented it is easy to change the solver of the collision operator. Usually, phonons do not have a single frequency; in [4] this simplification was set in order to directly compute the collision operator without needing to perform inter-

polations. In this method, we just have to add as many interpolations as the frequencies are. In [15] they took into account six frequencies, for a diode of total length 600 nm, with a channel of 400 nm. The collision operator transforms into

$$S(k,k') = \sum_{i=1}^{6} K_i \left[(n_{q_i}+1)\delta(\varepsilon(k')-\varepsilon(k)+\hbar\omega_i) + n_{q_i}\delta(\varepsilon(k')-\varepsilon(k)-\hbar\omega_i) \right] + K_0\delta(\varepsilon(k')-\varepsilon(k)). \tag{3.1}$$

In (3.1), n_{q_i} are the occupation numbers of phonons

$$n_{q_i} = \frac{1}{\exp\left(\frac{\hbar\omega_i}{k_B T_L}\right)-1}, \tag{3.2}$$

and the kernels K_i are

$$K_i = \frac{Z_f D_t k_i^2}{8\pi^2 \hbar \rho_0 \omega_i}, \tag{3.3}$$

where $\hbar\omega_i$ and $D_t k_i$ are the energy and the deformation potentials of the corresponding phonon type. The numerical results are shown in Figs. 13 and 14. The following doping profile is chosen:

$$N_D = \begin{cases} 5\times 10^{17}\ cm^{-3} & n^+\text{-zone} \\ 2\times 10^{15}\ cm^{-3} & n\text{-zone} \end{cases}$$

and the quantities related to the phonon frequencies are set

freq.	Z_f	$\hbar\omega(meV)$	$D_tK(10^8 eV/cm)$	freq.	Z_f	$\hbar\omega(meV)$	$D_tK(10^8 eV/cm)$
1	1	12	0.5	4	4	47.4	2
2	1	18.5	0.8	5	1	61.2	11
3	4	19	0.3	6	4	59	2

where Z_f is the number of equivalent valleys.

In this case, the use of the numerical scheme in [4] becomes much more involved leading to very fine grids in energy variables and interpolations like in our case. Moreover, we show in Fig. 13 the comparison of our results to the ones obtained with a simple application of the MultiGroup-WENO solver which are quite satisfactory. In [12], this technique was applied in case of a single phonon frequency; here, we consider multifrequency phonons. This requires only some simple modifications of the collision operator. Since the MultiGroup scheme is based on the cell average with respect to the wave vector, the presence of many delta distributions in the collision operator does not pose new difficulties. Also in this case our method allows for a good resolution of the pdf's in the k-space as shown in Fig. 14.

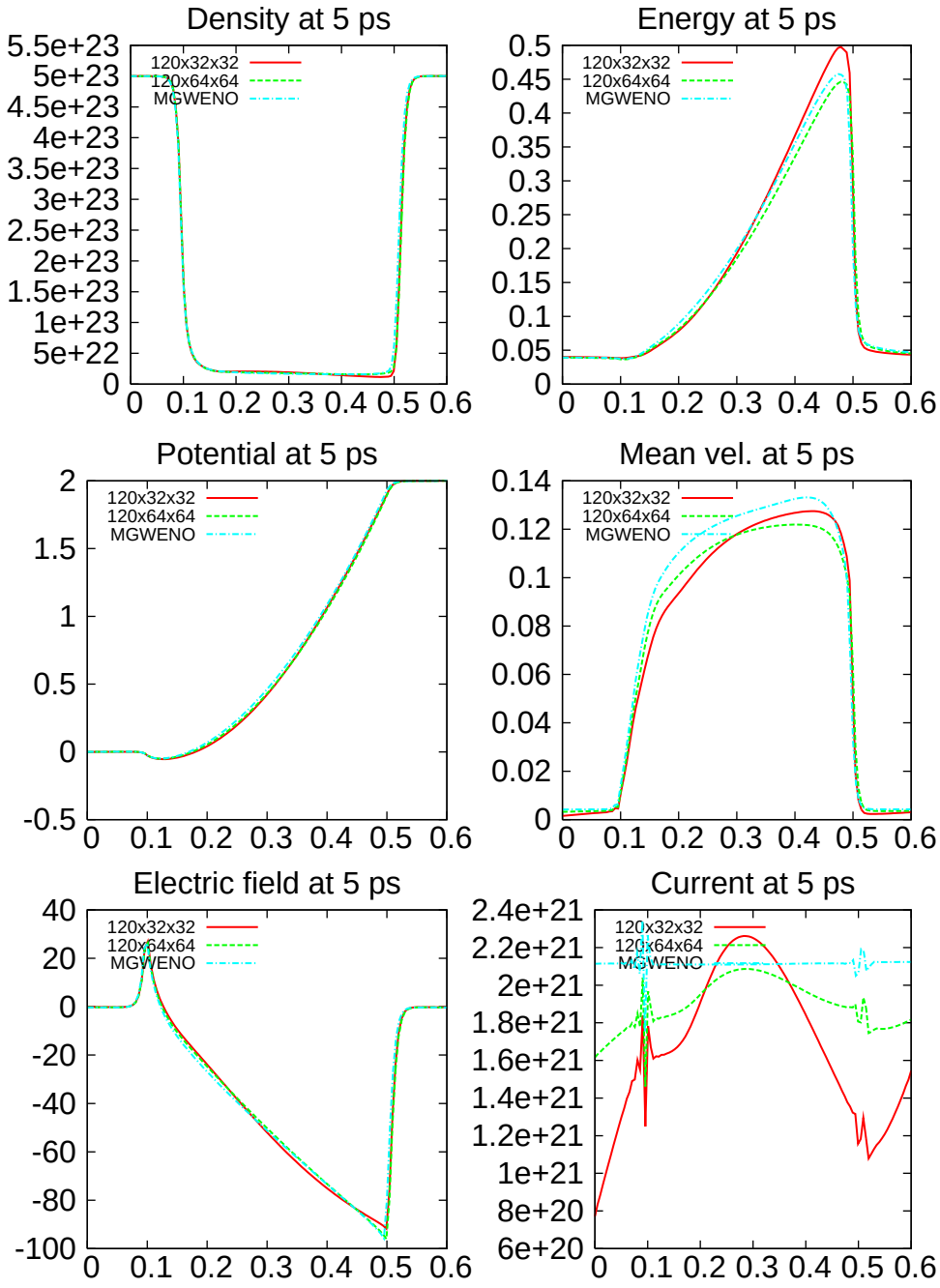

Figure 13: Macroscopic magnitudes given by the PW5TS method and a reference result obtained through a Multi-Group WENO scheme. For the PW5TS simulation The k-resolution is set $\bar{N}=27$, the time stepping is set $\Delta t=0.01ps$, 2nd order TS, linear interpolation for collisions.

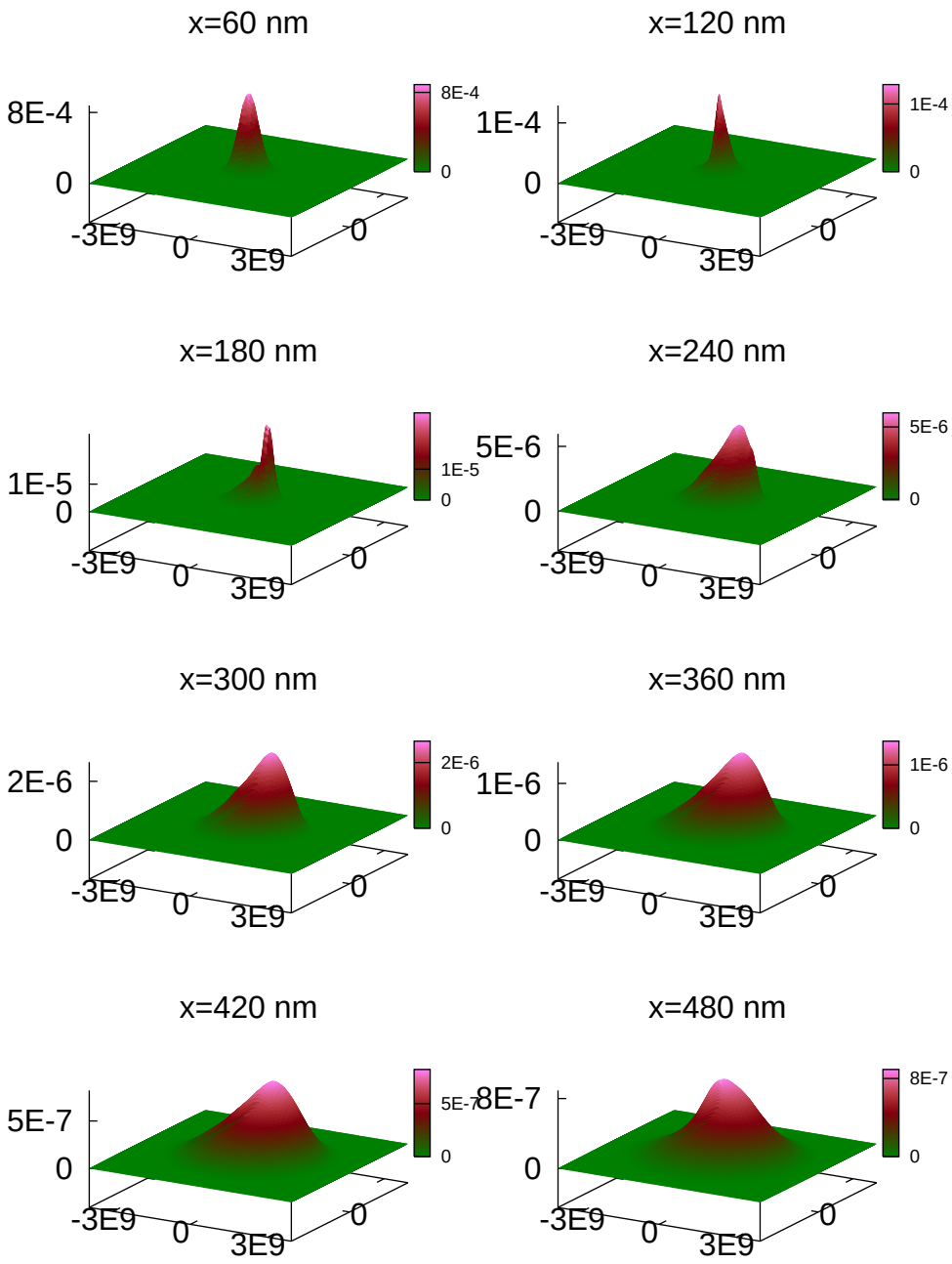

Figure 14: Snapshots given by the PW5TS method at different points of the multifrequency device, at time 5 ps. The grid is set $120\times64\times64$, $\bar{N}=27$, $\Delta t=0.01ps$, 2nd order TS, linear interpolation for collisions.

Acknowledgments

JAC and FV acknowledge support from DGI-MEC (Spain) FEDER project MTM2005-08024 and Grup Consolidat 2005SGR00611. AM acknowledges support from italian PRIN04.

Appendix

A.1 Adimensionalization summary

The BP system reads

$$\begin{cases} \dfrac{\partial f}{\partial t}+c_x\nabla_x\varepsilon\cdot\nabla_x f-c_k E\cdot\nabla_k f=\mathcal{Q}[f], \\ f_0(x,k)=c_{init}N_D(x)M(k), \end{cases}$$

where the energy-band function becomes $\varepsilon(k)=c_\varepsilon|k|^2$, and the Maxwellian

$$M(k)=\left(\frac{\pi}{C_M}\right)^{-3/2}e^{-C_M k^2}.$$

The electrostatic field is self-consistently computed through the Poisson's equation

$$\Delta_x\Phi=c_p[\rho(t,x)-N_D(x)],\qquad E=-c_e\nabla_x\Phi,$$

where the density is given by

$$\rho(t,x)=c_d\int_{\mathbb{R}^3}f(t,x,k)dk.$$

The gain and loss parts of the collision operator are

$$\mathcal{Q}^+[f]=\int_{\mathbb{R}^3}f(t,x,k)\left[c_0\delta(\varepsilon(k)-\varepsilon(k'))+c_+\delta\left(\varepsilon(k)-\varepsilon(k')+\frac{\hbar\omega}{\varepsilon^*}\right)+c_-\delta\left(\varepsilon(k)-\varepsilon(k')-\frac{\hbar\omega}{\varepsilon^*}\right)\right]dk'$$

and

$$\mathcal{Q}^-[f]=f(t,x,k)\int_{\mathbb{R}^3}\left[c_0\delta(\varepsilon(k)-\varepsilon(k'))+c_+\delta\left(\varepsilon(k)-\varepsilon(k')-\frac{\hbar\omega}{\varepsilon^*}\right)+c_-\delta\left(\varepsilon(k')-\varepsilon(k)+\frac{\hbar\omega}{\varepsilon^*}\right)\right]dk'.$$

The current is the first momentum in the k_1 direction,

$$j(x)=c_j\int_{\mathbb{R}^3}k_1 f(k)dk,$$

the mean velocity is $u(x)=c_u j(x)/\rho(x)$, and the energy is

$$W(x)=c_W\frac{1}{\rho(x)}\int_{\mathbb{R}^3}\varepsilon(k)f(k)dk.$$

The dimensionless parameters are derived from physical constants, the problem data and the adimensionalization parameters:

parameter	400 nm diode	50 nm diode	parameter	400 nm diode	50 nm diode
$c_\varepsilon = \frac{\hbar^2 k^{*2}}{2m^*\varepsilon^*}$	1	1	$C_M = \frac{\hbar^2 k^{*2}}{2m^* k_B T_L}$	1	1
$c_x = \frac{t^*\varepsilon^*}{\hbar k^* l^*}$	0.0842885	0.337154	$c_0 = \frac{K_0 t^* k^{*3}}{\varepsilon^*}$	0.265376	0.265376
$c_k = \frac{qt^*E^*}{\hbar k^*}$	0.326042	1.30417	$c_+ = \frac{Kt^*(n_q+1)k^{*3}}{\varepsilon^*}$	0.507132	0.507132
$c_d = \frac{k^{*3}}{\rho^*}$	1	1	$c_- = \frac{Kt^* n_q k^{*3}}{\varepsilon^*}$	0.0443372	0.0443372
$c_p = \frac{q\rho^* l^{*2}}{\epsilon V^*}$	156480	9780.02	$c_j = \frac{\hbar k^{*4}}{m^* j^*}$	1.70562×10^{7}	1.06601×10^{6}
$c_e = \frac{V^*}{l^* E^*}$	10	10	$c_u = \frac{j^*}{u^*\rho^*}$	9.88362×10^{-9}	6.32552×10^{-7}
$c_{init} = \frac{1}{c_d}$	1	1	$\frac{k^{*3}\varepsilon^*}{\rho^* W^*}$	4.14195×10^{-33}	6.62712×10^{-32}

The physical constants involved in the solution of the BP problem are:

name	meaning	value
$\hbar$	Dirac's constant	$\frac{6.626068\times10^{-34}}{2\pi}$ $=1.05456\times10^{-34}\frac{m^2 Kg}{s}$
q	elementary charge	1.60217646
m^*	effective electron mass $=0.32\times$ electron mass	$0.32\times9.10938188\times10^{-31}Kg$ $=2.915\times10^{-31}Kg$
k_B	Boltzmann's constant	$1.3806503\times10^{-23}\frac{m^2 Kg}{s^2 K}$
u_l	sound velocity	$9040\frac{m}{s}$
ρ_0	Si crystal density	$2330\frac{Kg}{m^3}$
ϵ_0	vacuum dielectric permittivity	$8.85419\times10^{-12}\frac{F}{m}$
ϵ_r	Si relative permittivity	11.7
ϵ	Si dielectric permittivity	$1.0359402\times10^{-10}\frac{F}{m}$
F	Farad	$F=\frac{s^4A^2}{m^2Kg}=\frac{C}{V}$

Finally, the problem data are:

$$\begin{cases} \omega = \text{frequency} = \dfrac{0.063eV}{\hbar} \\ D_t k = \text{optical coupling frequency} = 11.4\times10^{10}\dfrac{eV}{m} \\ K_0 = \dfrac{k_B T_L {E_{ac}}^2}{4\pi^2 h u_l^2 \rho_0} = 1.08638\times10^{-35} \\ E_{ac} = \text{deformation potential} = 9\ eV \\ K = \dfrac{D_t k^2}{8\pi^2\rho_0\omega} = 1.89456\times10^{-35} \\ T_L = \text{lattice temperature} = 300K. \end{cases}$$

A.2 Time splitting scheme

Combining all the time splittings, we get the following scheme: given the distribution function $f^n = f(t=t^n)$, we update f up to f^{n+1} by the following successive steps:

1. perform a $\Delta t/2$ step for transport

$$\frac{\partial f^n}{\partial t} + c_x \nabla_x \varepsilon \cdot \nabla_x f^n - c_E \cdot \nabla_k f^n = 0.$$

   1.1 perform a $\Delta t/4$ step for x-transport

$$\frac{\partial f^n}{\partial t} + c_x \nabla_x \varepsilon \cdot \nabla_x f^n = 0, \qquad f^{n+1/7} = [\Delta t/4;\, 0;\, 0],$$

   where and below [a; b; c] means that the corresponding x-transport is a, k-transport is b, and the collision is c.

   1.2 perform a $\Delta t/2$ step for k-transport

$$\frac{\partial f^{n+1/7}}{\partial t} - c_E \cdot \nabla_k f^{n+1/7} = 0, \qquad f^{n+2/7} = [\Delta t/4;\, \Delta t/2;\, 0].$$

   1.3 perform a $\Delta t/4$ step for x-transport

$$\frac{\partial f^{n+2/7}}{\partial t} + c_x \nabla_x \varepsilon \cdot \nabla_x f^{n+2/7} = 0, \qquad f^{n+3/7} = [\Delta t/2;\, \Delta t/2;\, 0].$$

2. perform a Δt step for collisions

$$\frac{\partial f^{n+3/7}}{\partial t} = \mathcal{Q}[f^{n+3/7}], \qquad f^{n+4/7} = [\Delta t/2;\, \Delta t/2;\, \Delta t].$$

3. perform a $\Delta t/2$ step for transport

$$\frac{\partial f^{n+4/7}}{\partial t} + c_x \nabla_x \varepsilon \cdot \nabla_x f^{n+4/7} - c_E \cdot \nabla_k f^{n+4/7} = 0.$$

   3.1 perform a $\Delta t/4$ step for x-transport

$$\frac{\partial f^{n+4/7}}{\partial t} + c_x \nabla_x \varepsilon \cdot \nabla_x f^{n+4/7} = 0, \qquad f^{n+5/7} = [3\Delta t/4;\, \Delta t/2;\, \Delta t].$$

   3.2 perform a $\Delta t/2$ step for k-transport

$$\frac{\partial f^{n+5/7}}{\partial t} - c_E \cdot \nabla_k f^{n+5/7} = 0, \qquad f^{n+6/7} = [3\Delta t/4;\, \Delta t;\, \Delta t].$$

   3.3 perform a $\Delta t/4$ step for x-transport

$$\frac{\partial f^{n+6/7}}{\partial t} + c_x \nabla_x \varepsilon \cdot \nabla_x f^{n+6/7} = 0, \qquad f^{n+1} = [\Delta t;\, \Delta t;\, \Delta t].$$

A.3 First-order time splitting scheme

The first-order time splitting scheme reads:

- **Step 1.** Solve $\frac{\partial f}{\partial t}+c_x\frac{\partial \varepsilon}{\partial k_1}\frac{\partial f}{\partial x}-c_k E_x\frac{\partial f}{\partial k_1}=0$ for a Δt-time step;
- **Step 2.** Solve $\frac{\partial f}{\partial t}=\mathcal{Q}[f]$ for a Δt-time step;

combined with a splitting of the same order for the solution of the transport part.

The scheme we obtain is:

1. perform a Δt step for transport

$$\frac{\partial f^n}{\partial t}+c_x\nabla_x\varepsilon\cdot\nabla_x f^n-c_E\cdot\nabla_k f^n=0.$$

   1.1 perform a Δt step for x-transport

$$\frac{\partial f^n}{\partial t}+c_x\nabla_x\varepsilon\cdot\nabla_x f^n=0,\qquad f^{n+1/3}=[\Delta t;\,0;\,0].$$

   1.2 perform a Δt step for k-transport

$$\frac{\partial f^{n+1/3}}{\partial t}-c_E\cdot\nabla_k f^{n+1/3}=0,\qquad f^{n+2/3}=[\Delta t;\,\Delta t;\,0].$$

2. perform a Δt step for collisions

$$\frac{\partial f^{n+2/3}}{\partial t}=\mathcal{Q}[f^{n+2/3}],\qquad f^{n+1}=[\Delta t;\,\Delta t;\,\Delta t].$$

References

[1] C. Auer, A. Majorana and F. Schürrer, Numerical schemes for solving the non-stationary Boltzmann-Poisson system for two-dimensional semiconductor devices, ESAIM: Proceedings, 15 (2005), 75-86.

[2] M. J. Cáceres, J. A. Carrillo and A. Majorana, Deterministic simulation of the Boltzmann-Poisson system in GaAs-based semiconductors, SIAM J. Sci. Comput., 27 (2006), 1981-2009.

[3] M. J. Cáceres, J. A. Carrillo, I. M. Gamba, A. Majorana and C.-W. Shu, Deterministic kinetic solvers for charged particle transport in semiconductor devices, in: C. Cercignani and E. Gabetta (Eds.), Transport Phenomena and Kinetic Theory: Applications to Gases, Semiconductors, Photons and Biological Systems, Series: Modelling and Simulation in Science, Engineering and Technology, Birkhäuser, 2007.

[4] J. A. Carrillo, I. M. Gamba, A. Majorana and C.-W. Shu, A WENO-solver for the transients of Boltzmann-Poisson system for semiconductor devices, Performance and comparisons with Monte Carlo methods, J. Comput. Phys., 184 (2003), 498-525.

[5] J. A. Carrillo, I. M. Gamba, A. Majorana and C.-W. Shu, 2D semiconductor device simulations by WENO-Boltzmann schemes: efficiency, boundary conditions and comparison to Monte Carlo methods, J. Comput. Phys., 214 (2006), 55-80.
[6] J. A. Carrillo and F. Vecil, Non oscillatory interpolation methods applied to Vlasov-based models, SIAM J. Sci. Comput, to appear.
[7] C. Z. Cheng and G. Knorr, The integration of the Vlasov equation in configuration space, J. Comput. Phys., 22 (1976), 330-348.
[8] F. Filbet and G. Russo, Accurate numerical methods for the Boltzmann equation, in: Modeling and Computational Methods for Kinetic Equations, Model. Simul. Sci. Eng. Technol., Birkhäuser Boston, Boston, 2004, pp. 117-145.
[9] F. Filbet, E. Sonnendrcker and P. Bertrand, Conservative numerical schemes for the Vlasov equation, J. Comput. Phys., 172 (2001), 166-187.
[10] M. Galler and F. Schürrer, A deterministic solver for the transport of the AlGaN/GaN 2D electron gas including hot-phonon and degeneracy effects, J. Comput. Phys., 210 (2005), 519-534.
[11] M. Galler, Multigroup equations for the description of the particle transport in semiconductors, Series on Advances in Mathematics for Applied Sciences 70, World Scientific Publishing, 2005.
[12] M. Galler and A. Majorana, Deterministic and stochastic simulations of electron transport in semiconductors, Bulletin of the Institute of Mathematics, Academia Sinica, 6th MAFPD (Kyoto) Special Issue, 2007.
[13] M. Galler and F. Schürrer, A direct multigroup-WENO solver for the 2D non-stationary Boltzmann-Poisson system for GaAs devices: GaAs-MESFET, J. Comput. Phys., 212 (2006), 778-797.
[14] G. S. Jiang and C.-W. Shu, Efficient implementation of weighted ENO schemes, J. Comput. Phys., 126 (1996), 202-228.
[15] A. Majorana, O. Muscato and C. Milazzo, Comparison of Monte Carlo and Boltzmann equation simulations for 1-D silicon devices, COMPEL, 23 (2004), 410-425.
[16] A. Majorana and R. M. Pidatella, A finite difference scheme solving the Boltzmann-Poisson system for semiconductor devices, J. Comput. Phys., 174 (2001), 649-668.
[17] P. A. Markowich, C. Ringhofer and C. Schmeiser, Semiconductor Equations, Springer-Verlag, New-York, 1990.
[18] C. Ringhofer, Space-time discretization of series expansion methods for the Boltzmann transport equation, SIAM J. Numer. Anal., 38 (2000), 442-465.
[19] C. Ringhofer, A mixed spectral-difference method for the steady state Boltzmann-Poisson system, SIAM J. Numer. Anal., 41 (2003), 64-89.
[20] L. Reggiani, Hot-electron transport in semiconductors, Topics in Applied Physics 58, Springer Verlag, Berlin, 1985.
[21] K. Sebastian and C.-W. Shu, Multidomain WENO finite difference method with interpolation at subdomain interfaces, J. Sci. Comput., 19 (2003), 405-438.
[22] C.-W. Shu and S. Osher, Efficient implementation of essentially non-oscillatory shock capturing schemes, J. Comput. Phys., 77 (1988), 439-471.
[23] G. Strang, On the construction and comparison of difference schemes, SIAM J. Numer. Anal., 5 (1968), 506-517.
[24] K. Tomizawa, Numerical Simulation of Submicron Semiconductor Devices, Artech House, Boston, 1983.